31 Jul 2023

A Spike-shaped Anchorage For Steel Reinforced Polymer (SRP)-strengthened Concrete Structures

Xingxing Zou

Keenan L. McBurney

Lesley H. Sneed
Missouri University of Science and Technology, sneedlh@mst.edu

Recommended Citation

A spike-shaped anchorage for steel reinforced polymer (SRP)-strengthened concrete structures

Xingxing Zou [a], Keenan L. McBurney [b], Lesley H. Sneed [c],[*]

[a] College of Civil Engineering, Nanjing Forestry University, Nanjing 210037, China
[b] Department of Civil, Architectural and Environmental Engineering, Missouri University of Science and Technology, Rolla, MO 65409 USA
[c] Department of Civil, Materials and Environmental Engineering, University of Illinois at Chicago, 929 W. Taylor St., Chicago, IL 60607 USA

ARTICLE INFO

ABSTRACT

Steel reinforced polymer (SRP) composite has recently emerged as an effective and economical solution for strengthening of reinforced concrete (RC) structures. Premature debonding failure of unanchored SRP at low load levels generally governs the performance of RC structures strengthened with externally bonded SRP. Therefore, a novel yet simple spike-shaped anchorage system was proposed in this study to prevent the debonding failure of SRP and to improve the interfacial shear capacity. Experimental investigation through single-lap shear tests of SRP-concrete joints showed that the anchorage system changed the failure mode from composite debonding to fiber rupture. In addition, the anchorage system substantially increased the peak load and reduced the interfacial slippage of the SRP-concrete joint compared to the unanchored condition. A numerical procedure based on the finite difference method was developed to predict the full-range load response, and results matched well with the full-range experimental responses of anchored and unanchored specimens. Parametric study of the test results and numerical simulation based on finite difference method both showed that the fiber rupture failure mode could be achieved for anchors in various positions along the bonded length. The closer the anchor is to the loaded end, the less global slip was obtained when the load reached the peak value.

1. Introduction

Fiber reinforced polymer (FRP) composite materials have the advantage of being high-strength and light-weight compared to traditional construction materials such as steel and concrete ([1,2]). Externally bonded (EB) FRP strips are an effective solution for the strengthening and rehabilitation of concrete structures since they provide external reinforcement [3]. Despite the well-established use of EB FRP with carbon or glass fibers, the growing interest in alternative fiber types has led to the introduction of those with lower cost and higher modulus. Among the "new generation" materials, the class of composites made of steel tapes has emerged as a promising and cost-effective solution for the external strengthening of concrete members ([4]). Typically, the steel tape consists of parallel high carbon steel wires within a micro-fine brass or galvanized coating ([5,6]). The steel wires are twisted around each other to form each individual cord or rope. A common configuration is the 3×2 cord, which is made of three straight wires, with another two twisted around them. The steel tapes can be applied in-situ via wet lay-up by using an epoxy resin, similar to FRP composite. The resulting system is known as SRP ("Steel Reinforced Polymer") ([7,8]).

Owing to the properties of the steel cords, SRP has high strength (typically larger than 2000 MPa), high-modulus (typically larger than 190 GPa), and non-linearity of strain at high stress levels, which results in several advantages compared with traditional carbon, glass, and basalt FRP: relatively higher stiffness, higher ductility, and less strength loss when bent or wrapped around sharp corners ([7,9]). Experimental and analytical investigations have shown that EB SRP can provide substantial additional flexural, shear, and axial strength to concrete structures ([8–12]).

Interfacial debonding has been proven to be one of the most critical causes of structural failure of EB FRP-strengthened concrete structures [1,13]. Likewise, researchers have consistently identified a limitation of the use of SRP to be debonding of the SRP in a brittle manner at low load levels ([7,14,15]). Debonding of FRP and SRP is generally the result of cohesive crack formation within the concrete substrate directly beneath the composite. Typically, debonding has been found to occur at strains considerably lower than the SRP tensile strain capacity [13]. In an

attempt to improve the strengthening solution and better utilize the composite material, it is herein hypothesized that anchorage devices may be installed in a similar manner as with anchored FRP-strengthened concrete structures ([16–25]). In fact, the higher strength of SRP perpendicular to the steel fiber longitudinal direction is appealing since it enables the fibers to be bent and anchored more effectively compared to glass or carbon FRP materials [13].

Currently, information about the anchorage of SRP is extremely limited in the literature. However, there are many effective means to anchor FRP, such as FRP anchors, U-jackets, and nailed plates [21]. Anchors for FRP work effectively by suppressing debonding failures and enabling strengthened members to achieve greater deformability and load carrying capacity in certain cases [15]. Mostofinejad and Mahmoudabadi [16] increased the total adhesive area between FRP and concrete by grooving the concrete surface before applying epoxy. Zhang et al. [17] added shear keys with FRP plates to increase the interlocking effect. Recently, a spike-shaped or fan-shaped anchor was investigated by several researchers ([18,19]). Spike-shaped FRP anchors are relatively inexpensive, and their installation is flexible and easy. When used with FRP laminates, the laminates do not have to be furnished with costly installation holes, which reduce the cross-section and cause notch effects. The load is transferred directly from the FRP laminate via the integrated FRP anchor to the concrete substrate without any slip between laminate and anchor. As a result, this anchorage solution does not rely on prestressing of anchors, and all anchors are engaged at low load levels [22].

Inspired by the design of spike-shaped anchors for FRP, this study aimed to develop an effective spike-shaped anchorage system for SRP that can increase the capacity and deformability at debonding or even mitigate the debonding failure mode. In order to investigate the effect of the anchors on the bond behavior of SRP-concrete interface, direct shear tests were conducted in which the primary test parameter was the anchor location along the bonded length. Secondary test parameters including the anchor embedment depth and overlap length were also examined. A numerical procedure was developed to predict and study the full-range load response of unanchored and anchored SRP-concrete joints subjected to direct shear.

2. Conception of steel fiber spike-shaped anchorage system for SRP

The conception of a steel fiber spike-shaped anchorage system for SRP is illustrated by an example of a reinforced concrete (RC) beam strengthened in flexure shown in Fig. 1. The SRP system is externally bonded to the flexural tension (bottom) surface of the RC beam. It has been shown that, with the increase of the applied load, SRP-concrete debonding may occur at two locations along the beam: (i) at the SRP ends resulting in concrete cover detachment or SRP-concrete delamination, or (ii) in the middle of the bonded area in regions of flexural cracks (Fig. 1). Debonding at the end of the strip is termed plate end (PE) debonding. Debonding in the middle of the beam is termed intermediate crack-induced (IC) debonding [26], which is one of the most dominant failure modes associated with the SRP bonding technique [7,27].

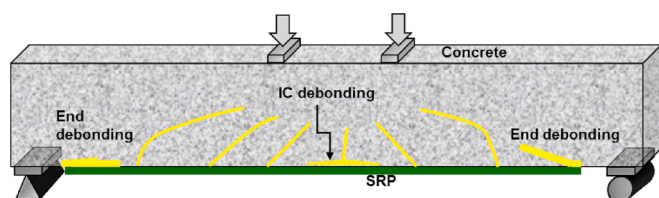Fig. 2 shows the design of the novel anchorage system that can be installed both at the ends and along the length of the SRP strip. The end anchorage, intended to prevent PE debonding, resists the normal stress and excessive interfacial slip at the SRP strip ends [28]. The end anchors are designed as a continuation of the bonded length of the SRP strip. The steel fiber bundles are bent at the designated end location of the bonded region, with the bent part merged together and embedded into pre-drilled holes with prefilled resin in the concrete substrate. The anchors along the length of the SRP strip, intended to prevent IC debonding, are designed like the spike anchors used in FRP-strengthened concrete systems [19,20]. Steel fiber bundles are cut and bent to an "L" shape as shown in Fig. 2, with one leg merged together and embedded into pre-drilled holes with prefilled resin in the concrete substrate. The other leg is overlapped and bonded together with the SRP bonded length.

Fig. 3 shows the design of the novel anchorage system for shear strengthening of an RC beam. The SRP strips are bonded to both sides of the beam, with the fiber direction perpendicular to the beam span direction. The anchors can be installed into the side of a beam with a rectangular cross section (Fig. 3a), or into flange of a beam with a T-shaped cross section (Fig. 3b).

3. Materials

3.1. Concrete

The concrete used to cast the single-lap direct shear test specimens was produced from normal weight dolomitic limestone coarse aggregate having a maximum size of 16 mm, natural river sand, and commercial Portland Type I/II cement. The concrete mixture had a target compressive strength of 30 MPa to represent concrete used in existing civil structures in need of strengthening. The mixture proportions by mass ratio were (cement: sand: aggregate) = (1:00: 3.33: 2.51), and the water-cement ratio was selected as 0.59.

Hardened concrete properties were tested using concrete cylinders cast from the same batch of concrete used to cast the single-lap shear test specimens. All concrete cylinders were cured under a plastic sheet for 24 h before being removed from the forms. After removing the forms, the cylinders were placed in a moist cure room for 28 days. During the curing of specimens, the room temperature was approximately 15 °C. The 28-day concrete compressive and splitting tensile strengths were obtained experimentally using 101.6 mm diameter × 203.2 mm long cylinders in accordance with ASTM C39/C39M [29] and ASTM C496/C496M [30], respectively. The compressive and splitting tensile strengths, each determined as the average of three tests, were 25.8 MPa (CoV = 0.08) and 2.45 MPa (CoV = 0.07), respectively. The tested compressive strength was lower than the design value, which could be due to the curing conditions.

3.2. Polymeric matrix

The polymeric matrix used in the SRP composite was a thixotropic epoxy [31]. The tensile strength, shear strength, and secant Young's modulus were > 14 MPa, > 20 MPa, and > 5.3 GPa, respectively, according to the manufacturer [31]. Additional details are presented in [13].

3.3. Steel fibers

The fibers used in the SRP composite were made of unidirectional high strength steel cords (Fig. 4). Each cord had a cross-sectional area (A_{cord}) of 0.538 mm^2 and consisted of five wires twisted together. Three straight wires formed the core of the cord, and two wires were twisted around them in a helical manner (Fig. 4). The wires were galvanized with a zinc coating and were laid on a fiberglass mesh backing.

Different fiber sheet densities, defined in terms of net steel fiber weight per unit fiber sheet area (in g/m^2), can be achieved by different cord spacings. One fiber sheet density was tested in this study, referred to herein as medium density (MD) fibers. All tests in this study were
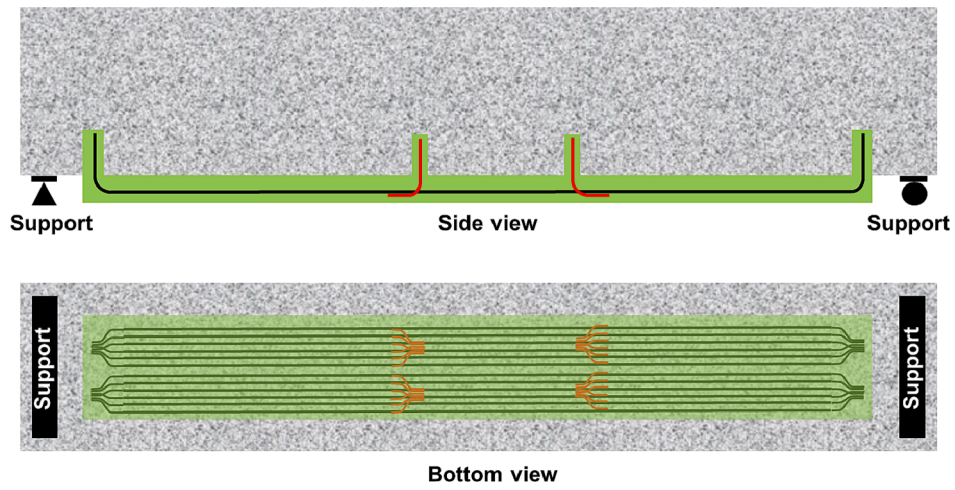

Fig. 1. Illustration of interfacial debonding of an SRP composite applied to the flexural tension surface of an RC beam.

Fig. 2. Design of the novel anchorage system for SRP flexural strengthening of an RC beam.
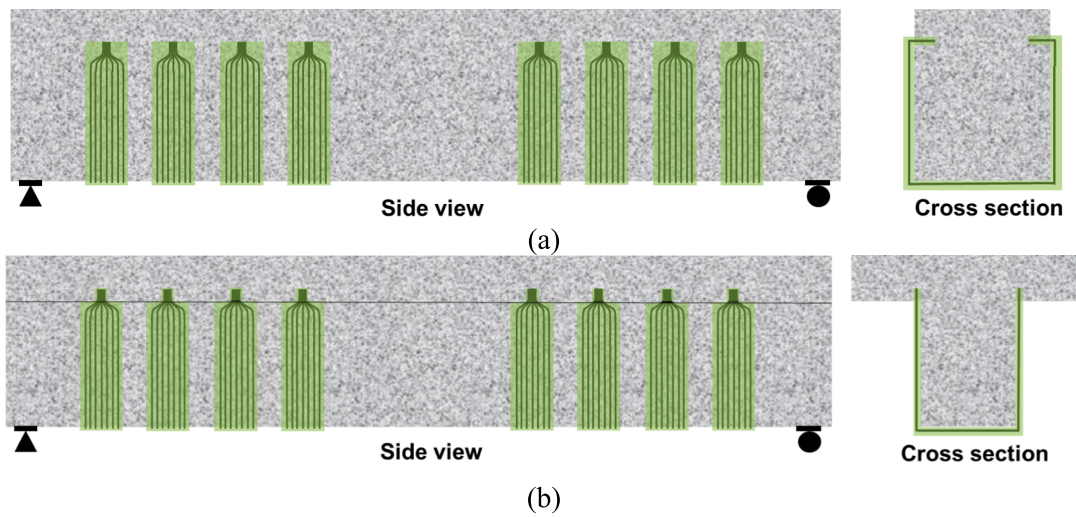

(a)

(b)

Fig. 3. Design of the novel anchorage system for shear strengthening of an RC beam: (a) rectangular cross section, and (b) T-shaped cross section.

Tensile strength > 3000 MPa

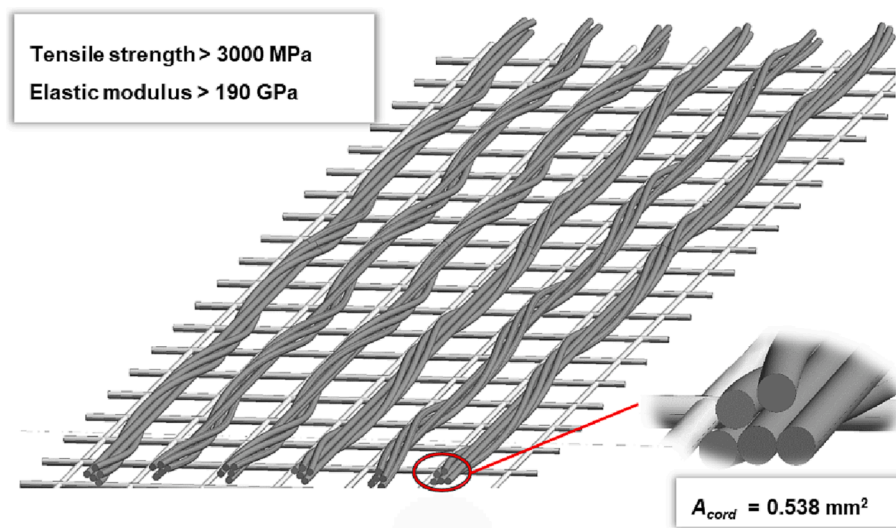Elastic modulus > 190 GPa

$A_{cord} = 0.538 \text{ mm}^2$

Fig. 4. Illustration of steel fiber sheet.

conducted using MD fibers because previous tests conducted by the authors [13] showed that unanchored SRP-concrete direct shear test specimens with MD fibers achieved the desired failure mode (composite debonding), whereas similar specimens with lower sheet density failed due to fiber rupture. The geometric and mechanical properties of the MD fiber sheet provided by the manufacturer [31] are summarized in Table 1.

To confirm the mechanical properties of the fibers, three MD bare fiber tensile coupons with 15 steel cords were tested in uniaxial tension, see Fig. 5a. As explained in detail in [13], the average elastic modulus, taken as the secant modulus at 5 kN of the tensile coupons, for the MD bare fiber sheet was 190.8 GPa (CoV = 0.05). The tensile strength of the MD bare fiber tensile coupons (each with a total of 15 cords) was 23.89 kN, and the corresponding mode of failure was fiber rupture. More details can be found in [13].

3.4. SRP plate

Four 50 mm wide $\times$ 4 mm thick (nominal) SRP tensile coupons consisting of MD fiber sheets with 15 steel cords embedded in the polymeric matrix were fabricated and tested in uniaxial tension (Fig. 5b). The applied load-axial strain response for a typical specimen is plotted in Fig. 5c, which shows that the stress–strain behavior was nonlinear due to the formation of transverse cracks in the matrix. Additional discussion on the stress–strain behavior of the SRP tensile specimens is reported in [13]. Similar to the bare fiber tensile test discussed in Section 3.3, the secant slope at 5 kN was taken as the elastic modulus of the SRP plate, E_f. It should be noted that the E_f of the SRP was determined with respect to the equivalent thickness of the fibers (t_f, see Table 1) for comparison with values reported in previous studies [15] and for use in calculations later in this paper. The average E_f for the SRP tensile coupons with MD fibers was 257.2 GPa (CoV = 0.08). This value is consistent with the value given by similar tests of SRP plates with the same fibers and polymer reported in [15]. The average tensile strength of the MD SRP plate tensile coupons was 21.60 kN, and the corresponding mode of failure was fiber rupture.

4. Methods

4.1. Specimen design

Single-lap direct shear tests were conducted to study the effect of anchors on the interfacial shear behavior of the SRP-concrete interface (Fig. 6). Each test specimen comprised an SRP plate bonded to the surface of a concrete block. The composite bonded area of all specimens was nominally the same. The bonded length was 240 mm and was designed to be longer than the effective bond length, defined as the minimum length required to fully develop the stress transfer zone (STZ), reported in [13] as 118 mm for the same composite and concrete in the present study. The bonded width was 50 mm, corresponding to 15 steel cords in the transversal (width) direction. The dimensions are shown in Fig. 6a.

A total of eight specimens were tested in this study. Two identical control specimens (C_1 and C_2) were cast without anchors, and the remaining six specimens (S_80_1, S_80_2, S_80_3, S_160, S_End_1, and S_End_2) were designed with anchors. Each of the anchored specimens included two anchors located at the same position along the composite

bonded length. Different parameters were varied, namely the anchor position along the bonded length (distance from the loaded end is denoted by L_A, see Fig. 6), overlap length along the bonded length (denoted by d_1, see Fig. 6), and anchor embedment length (denoted by d_2, see Fig. 6). Values of d_1 and d_2 were selected based on review of research on FRP spike anchors reported in the literature [20]. The specimens and their corresponding parameters are summarized in Table 2.

4.2. Specimen construction

The concrete prisms were 125 mm wide $\times$ 125 mm deep $\times$ 375 mm long, with the same dimensions as those used in [13]. The concrete prisms were constructed in custom timber formwork and were cured in the same manner as the concrete cylinders used for the material property tests, as discussed in Section 3.1. After curing was completed, the prisms were stored in the laboratory where they were tested approximately two months later.

The side faces of the concrete prisms were sandblasted to expose the coarse aggregates prior to the application of the composite, see Fig. 7a. For each specimen with anchors, two 12 mm diameter holes (Fig. 7b and 7c) were drilled into the concrete prism at predefined locations designed in Table 2 and Fig. 6. The hole depth was 60 mm, which was slightly longer than the length of the embedded part of the anchors. Excess dust and debris were removed from the holes with compressed air and a shop vacuum. The holes were then cleaned with alcohol one day before filling in resins.

For specimens with anchors along the bonded length, i.e., specimens S_80_1, S_80_2, S_80_3, and S_160, the anchors were formed using a precut strip fiber sheet having the same width (and number of cords) as the bonded strip. The anchor strip was bent into an L-shape, and the bare fibers were inserted through the main strip after the mesh backing was removed Fig. 8a and 8b. Then, approximately half of the fibers were gathered together and inserted into each hole with prefilled fresh resin. For specimens with end anchors, i.e., specimens S_End_1 and S_End_2, the fiber strip was cut to include the length needed for the anchors. The strip was bend into an L-shape at the location of the end anchors, and the mesh backing was removed along the anchor length (see Fig. 8c). Approximately half the fibers were gathered together and inserted into each hole with prefilled fresh resin.

The SRP composite was installed using a wet layup process. Steel plates and foam board were used as forms to control the bonded area of the SRP composite and the thickness (Fig. 7c). After 72 h, the forms were removed (Fig. 7d).

4.3. Test setup

Approximately one week after removing the forms used to install the SRP composite, the specimens were tested in single-lap shear using a near-end supported test setup. The concrete specimen was mounted onto the base of the 250 kN uniaxial servo-hydraulic universal testing machine using the same test fixture as in the tests reported in [13] (Fig. 6). Metal plates were attached to the gripped end of the SRP strip using thermosetting epoxy adhesive and bolts in each corner of the plates. The bolts were tightened to allow for better gripping during testing and to reduce the likelihood of the steel fibers or SRP plate from slipping between the plates during testing (Fig. 6). Brackets were attached to the concrete surface to hold two LVDTs aligned with the SRP fibers during the test procedure. An Ω-shaped, cold-formed metal plate was mounted onto the SRP strip at the loaded end of the bond length (Fig. 6). The Ω-plate was used as a reaction surface for the LVDTs. The load was applied via displacement control by monotonically increasing the average reading of the two LVDTs at a fixed rate of 0.00084 mm/s, which is consistent with the previous study by the authors reported in [13]. The average reading of the two LVDTs was considered as the slip at the composite loaded end (referred to herein as the global slip, g) of the

Table 1
Properties of medium density (MD) fibers provided by the manufacturer [31].

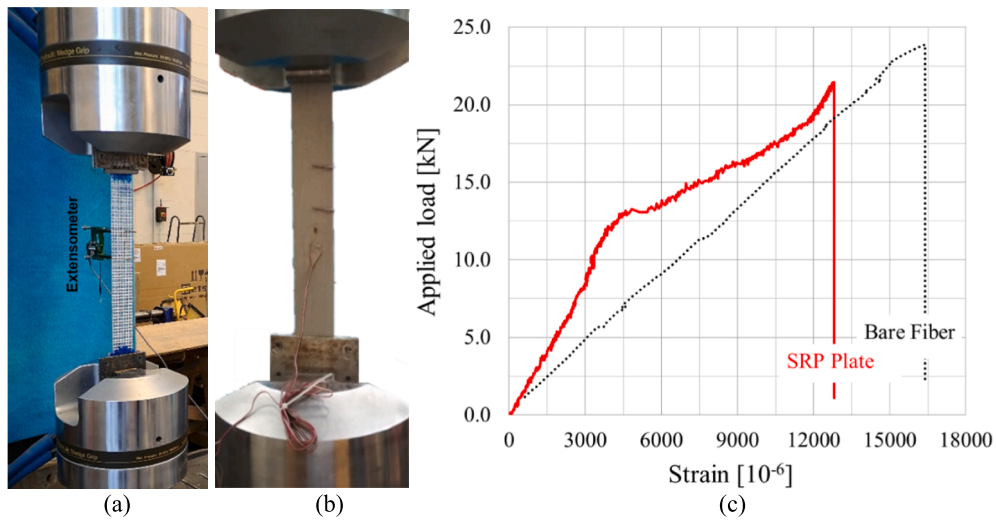| Density of fiber sheets (g/m²)	Number of cords (/mm)	Equivalent thickness t_f (mm)	Break deformation (%)	Tensile strength (MPa)	Elastic modulus (GPa)
1200	0.314	0.169	>2	>3000	>190

Fig. 5. Tensile test: (a) bare steel fiber sheet, (b) SRP plate, and (c) applied load vs. tensile strain results of bare steel fiber sheet and SRP plate.
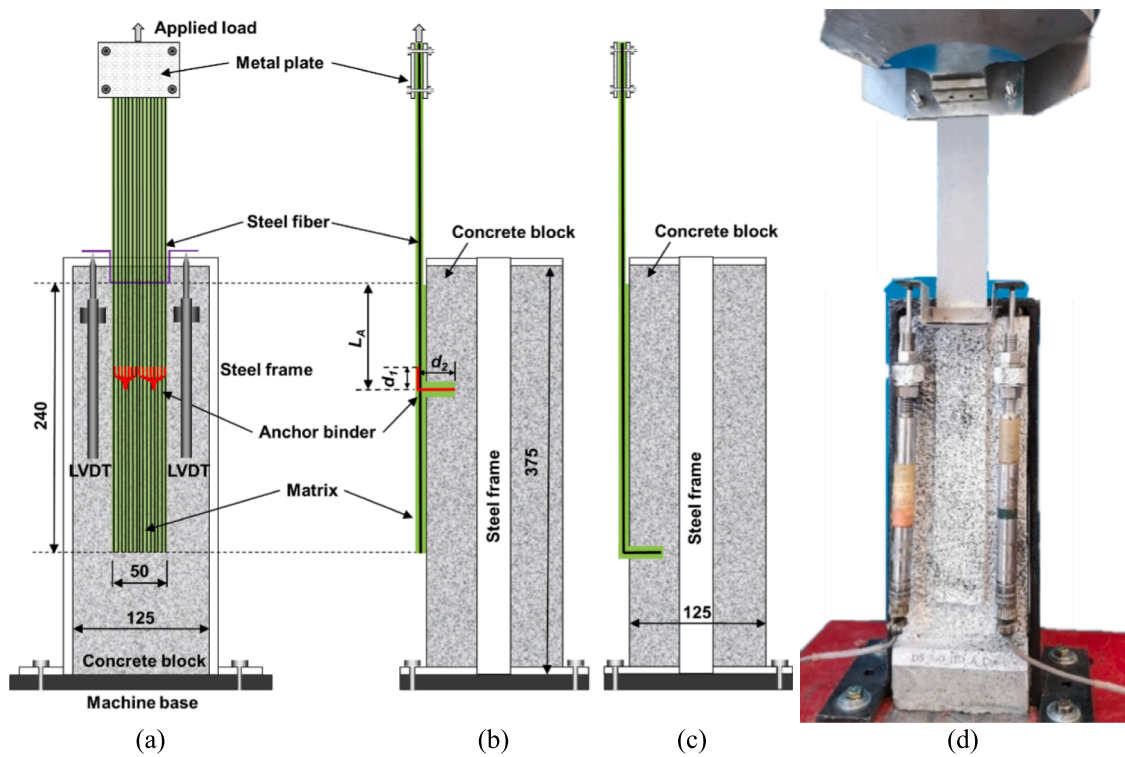

Fig. 6. Single-lap shear test specimen: (a) front view, (b) side view showing anchors located along the composite bonded length, (c) side view showing anchors at the composite unloaded end, and (d) photo of test specimen. (Units in mm).

Table 2
Summary of test specimens and test results.

Specimen	Anchor	L_A (mm)	d_1 (mm)	d_2 (mm)	Failure Mode	P_{max} (kN)	g_{ult} (mm)
C_1	No	–	–	–	Debonding	16.08	1.722
C_2	No	–	–	–	Debonding	16.22	1.851
S_80_1	Yes	80	50	50	Fiber rupture	23.10	0.584
S_80_2	Yes	80	30	50	Fiber rupture	23.77	0.642
S_80_3	Yes	80	50	30	Fiber rupture	23.94	0.801
S_160	Yes	160	50	50	Fiber rupture	22.38	2.247
S_End_1	Yes	240	50	50	Fiber rupture	24.86	2.394
S_End_2	Yes	240	50	50	Fiber rupture	23.99	2.529
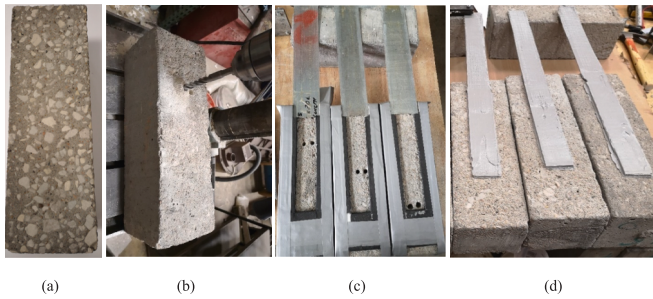
Fig. 7. Construction of test specimen: (a) sandblasted concrete prism, (b) drilling holes for anchors, (c) epoxy formwork, and (d) anchored SRP composite strips bonded to prism (specimens shown have anchors located 80 or 160 mm from loaded end).

fibers relative to concrete prism. Digital image correlation (DIC) was employed on all specimens to determine the axial strain along the fiber direction on the surface of the SRP. A Sonyα6000 camera was triggered at a selected frequency to obtain images. The images were analyzed using a DIC software package [32]. The specimens were tested until one of the following criteria was reached: the composite failed due to complete detachment, or the applied load dropped to near-zero (loss of load-carrying capacity).

5. Experimental results and discussion

5.1. Failure mode

5.1.1. Control specimens
The two control specimens experienced the failure mode of SRP

debonding, which occurred within the concrete adjacent to the adhesive-concrete interface. This failure mode was consistent with that of many similar specimens in the previous study by the authors [13]. At failure, the SRP strip completely detached from the concrete prism, with a thin layer of concrete attached to the SRP strip (Fig. 9). This type of failure is not strictly 'debonding' because the failure is associated with fracture of the concrete substrate. Nevertheless, the term is adopted herein because it has been widely used in many studies regarding to this topic [33,34]. The thickness of the concrete layer on the debonded SRP strip varied between approximately 1 and 3 mm. The surface of the failure zone of the concrete prism was uneven, with the aggregate being clearly visible (Fig. 9c).

5.1.2. Anchored specimens
All anchored specimens failed due to rupture of the steel fibers (Fig. 10). The rupture process occurred progressively and rapidly, sometimes less than several seconds. At failure, specimen S_End_1 exhibited separation between the SRP and concrete, although close inspection after unloading showed local fiber rupture at the bonded region close to the anchored end. For all anchored specimens in this study, fiber rupture occurred along the straight portion of the fiber sheet and not at the bend location.

5.2. Load response

Fig. 11 shows the load responses of all specimens. The sections that follow discuss the behavior of the control and anchored specimens.

5.2.1. Control specimens
The load response of both control specimens, namely specimens C_1 and C_2, was similar as shown in Fig. 11. Fig. 12a shows the relationship

(a)

(b)

(c)
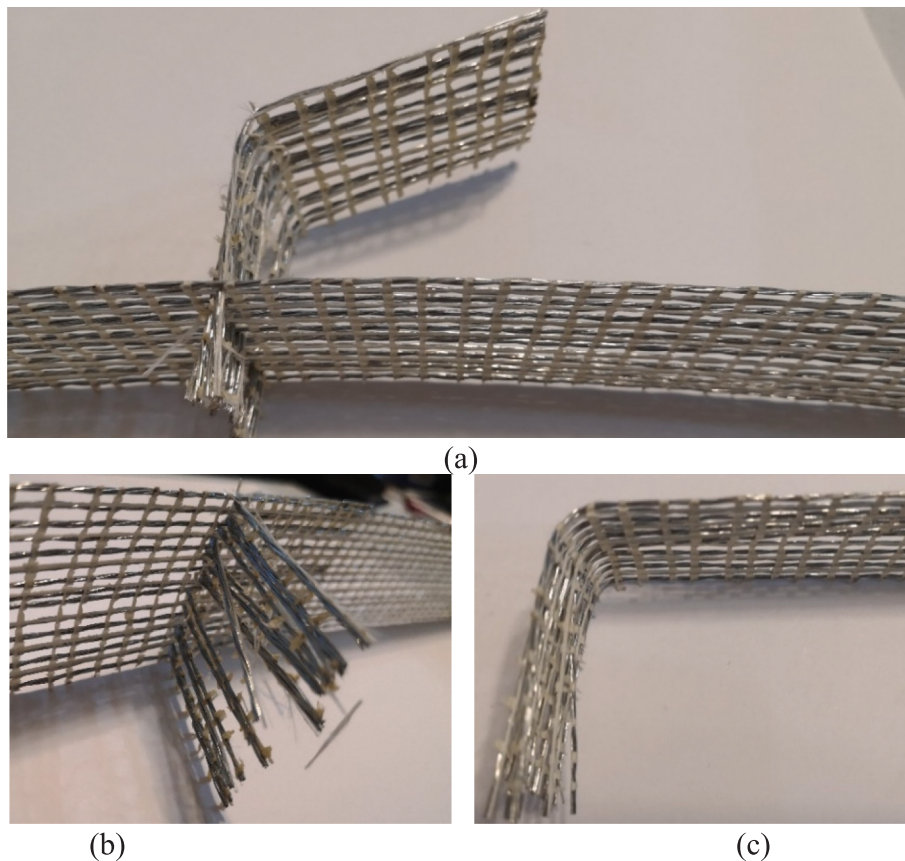
Fig. 8. Formation of anchors: (a) bent fiber strip of the anchors located along the composite bonded length, (b) close-up view of fibers inserted through the fiber strip, (c) bent fibers of the end anchors.
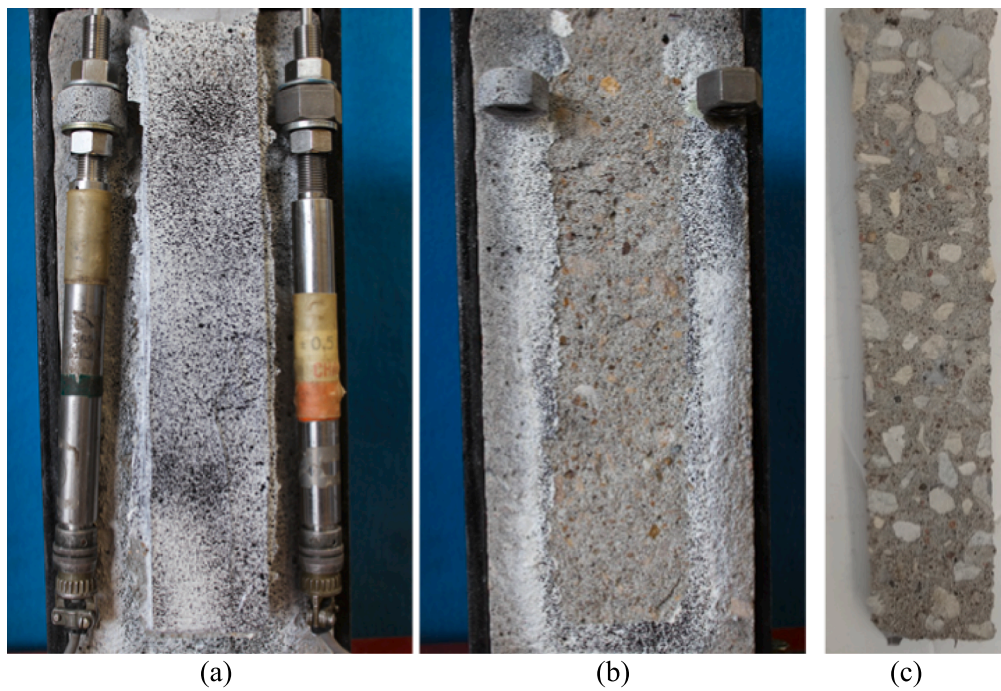
Fig. 9. Failure mode of control specimen C_1: (a) SRP plate separated from concrete substrate, (b) concrete substrate surface, and (c) back of SRP plate after debonding.
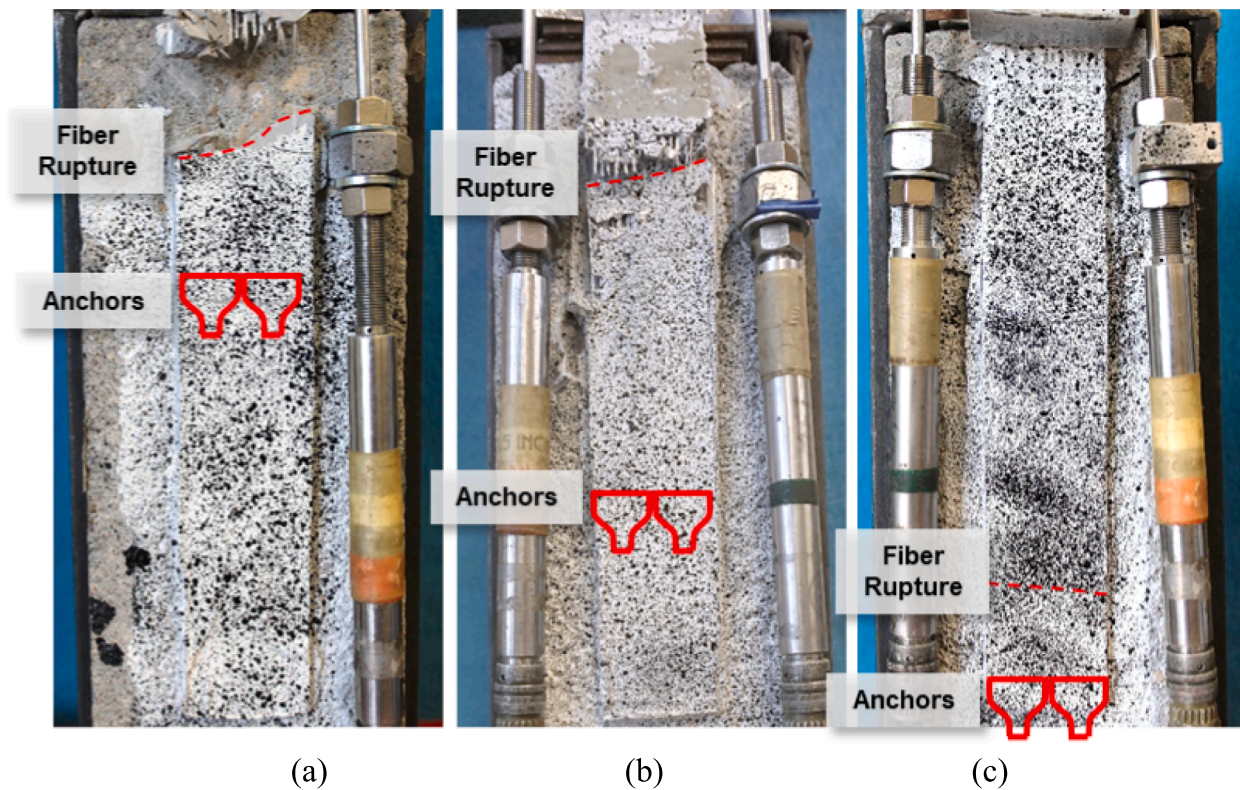
Fig. 10. Failure mode of anchored specimens: (a) fiber rupture of specimen S_80_1, (b) fiber rupture of specimen S_160, and (c) SRP-concrete separation of specimen S_End_1 (fiber rupture occurred behind SRP plate).

between the applied load and the global slip for control specimen C_2 and highlights key points along the response. An initial linear response was followed by a non-linear branch until a relatively larger load, corresponding to Point A, was reached. A drop in the load from Point A to Point B marked the onset of the interfacial crack propagation [15,35]. As the crack propagated, the load remained nearly constant with fluctuations until failure.

From the beginning of loading until failure, no obvious cracks were observed in the concrete substrate. However, one salient difference between SRP- and FRP-concrete joints is that the SRP strips displayed

Fig. 11. Load responses of specimens.

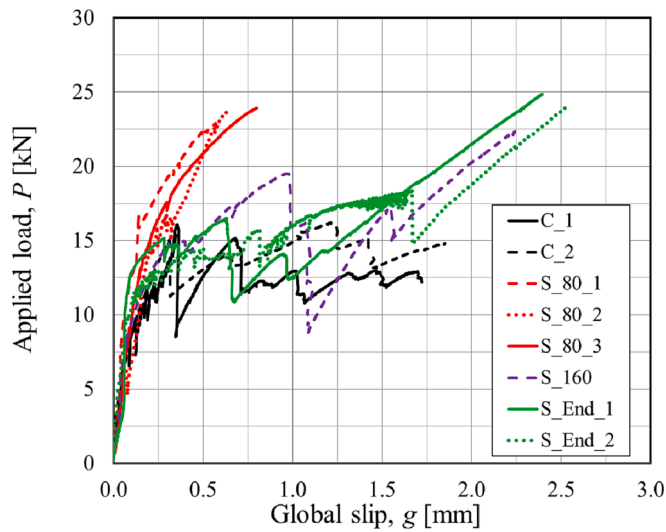multi-cracking behavior along the transversal direction of fibers (illustrated in Fig. 12b), which is similar to the behavior observed in the SRP plate tensile tests described in Section 3.4. As the progressive debonding occurred from the composite loaded end to the unloaded end, the transversal cracks occurred near the loaded end first, and then additional cracks occurred with the increase of global slip. Fig. 12b shows the location of the first crack, which formed at the region close to the

loaded end, at Point A of the load response. After the first crack, there was a notable load drop, then the load increased again until another crack formed. This behavior continued until Point M, which was just before failure of the specimen.

5.2.2. Anchored specimens

As discussed in Section 3.4, the anchored specimens shared a similar failure mode of fiber rupture (Fig. 10). The load responses of anchored specimens S_80_1, S_80_2, S_80_3, with anchors near the loaded end, were almost the same (see Fig. 11). Fig. 13 details the load response of Specimen S_80_3, which is representative of the three specimens in that series, although they had different combinations of anchor embedment and overlap lengths. At the beginning of loading, the load increased nearly linearly, similar to the initial response of the control specimens. Then the load continued to increase at a gradually decreasing slope until failure (Fig. 13a). The global slip at failure of these three specimens was approximately 0.7 mm, much less than the other anchored specimens with anchors farther from the loaded end. The peak load of these specimens (around 23 kN) was similar to (within 6% of) the ultimate load of the SRP plate specimens (21.60 kN, as discussed in Section 3.4) with the same fiber density tested in uniaxial tension and that failed in fiber rupture. The axial strain response (Fig. 13b) shows that debonding and matrix cracking progressed from the loaded end to the anchor location until failure. The bonded area between the anchor location and the unloaded end had little to no cracks indicating a low stress zone.

The load responses of anchored specimens S_160, S_End_1, and S_End_2, with anchors farther away from the load end, were similar to one another. Fig. 14 shows the load response of specimen S_160. First, the load increased approximately linearly to around 15 kN (Point A in

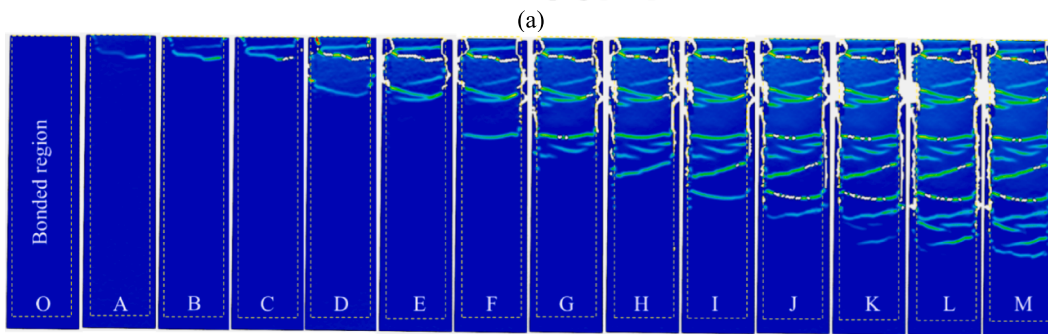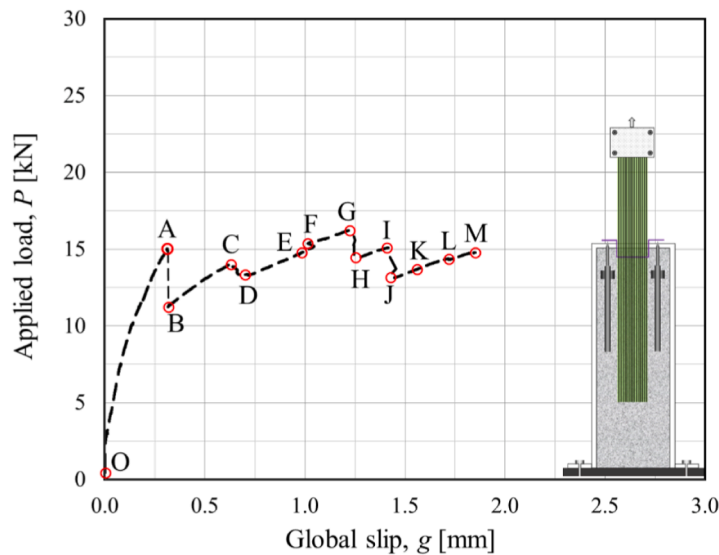

(a)

(b)

Fig. 12. Load response of control specimen C_2: (a) applied load-global slip response, and (b) illustration of axial strain measured by DIC at different points on the applied load-global slip response.

Fig. 13. Load response of anchored specimen S_80_3: (a) applied load-global slip response, and (b) illustration of axial strain measured by DIC at different points on the applied load-global slip response.
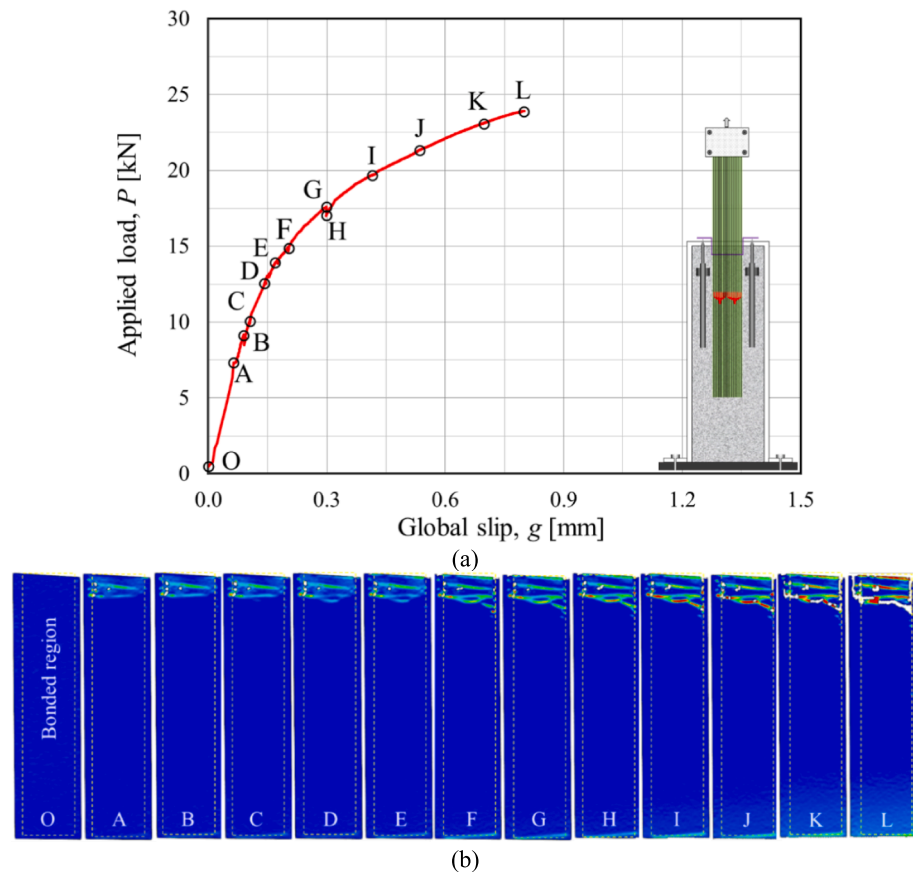
Fig. 14a). Then, the load increased nonlinearly at a decreasing slope with occasional slight load drops until Point E in Fig. 14a. Following, there was a larger load drop, and then the load increased gradually until fiber rupture failure occurred. The axial strain response (Fig. 14b) shows that debonding and transversal cracking progressed from the loaded end to the anchor location until failure. The formation of new cracks caused sudden load drops, see Point E-F or Point K-L in Fig. 14. Similar to Fig. 13b, the region beyond the anchors had very low strain response, and no cracks were observed in Fig. 14b.

Fig. 15 shows the load response of specimen S_End_1. First, the load increased approximately linearly to around 10 kN. Then, the load increased nonlinearly at a decreasing slope with occasional load drops. Audible cracking sounds were documented at the load drops. When the global slip reached around 1.7 mm, there was a load drop, and then the load increased linearly until fiber rupture failure occurred. The ultimate slip of these three specimens was approximately 2.0–2.6 mm. The axial strain response (Fig. 15b) shows that debonding and transversal cracking progressed from the loaded end to the anchor location until failure. Each new crack caused a sudden load drop, see Point H-I or Point J-K in Fig. 15.

5.3. Effect of anchors

Comparing the load responses in Fig. 11, it can be seen that near-end anchored specimens S_80_1, S_80_2, and S_80_3 had a different load response from that of the control (unanchored) specimens C_1 and C_2; the near-end anchored specimens demonstrated an initial increasing response similar to the control specimens that transitioned smoothly to a linearly-increasing response controlled by the steel fibers until failure. The load response of these specimens was controlled mainly by the fibers

until failure. Additionally, Fig. 11 shows that the effect of the anchor depth and fiber overlap length on the load response was insignificant for the near-end anchored specimens in this study. Specimens with anchors positioned farther away from the loaded end (namely specimens S_160, S_End_1, and S_End_2) demonstrated an initial increasing load response similar to the control specimens, followed by a near-constant load branch with similar fluctuations in load until the corresponding point of failure in the control specimens, after which the load increased approximately linearly until failure. The load response of these specimens was controlled by the composite and substrate until the composite debonded between the loaded end and the anchors, after which the load response was controlled by the fibers until failure.

The peak load, P_{max}, achieved by each specimen is listed in Table 2 and is shown in Fig. 16a. The anchored specimens experienced an increase in peak load of about 6 to 8 kN compared to the unanchored (control) specimens, or about a 40% to 50% increase. This is because failure of the unanchored specimens was controlled by debonding, in particular, fracture of a thin concrete layer adjacent to the interfacial adhesive, while failure of the anchored specimens was controlled by fiber rupture. In this case, the percent increase in peak load due to the anchors (i.e., the efficiency of the anchors) represents a lower bound, since the control specimens in this study had a bonded length that was sufficient to fully develop the STZ. Unanchored specimens with a bonded length less than the effective bond length would be expected to fail due to debonding at a lower peak load, and therefore would be expected to have a larger percent increase in peak load with the addition of anchors. Additionally, results in Table 2 and Fig. 16a indicate that the location of the anchorage along the bonded length did not affect the peak load, as the differences displayed are not significant and can be attributed to differences that could not be controlled during fabrication.
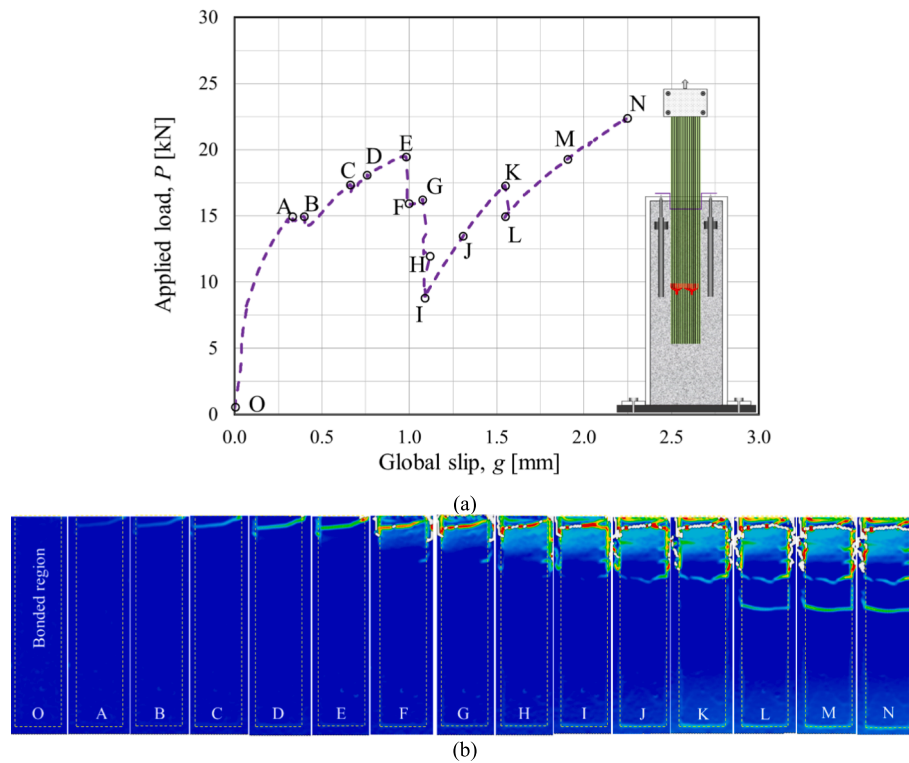
Fig. 14. Load response of anchored specimen S_160: (a) applied load-global slip response, and (b) illustration of axial strain measured by DIC at points on the applied load-global slip response.

Fig. 15. Load response of anchored specimen S_End_1: (a) applied load-global slip response, and (b) illustration of axial strain measured by DIC at points on the applied load-global slip response.
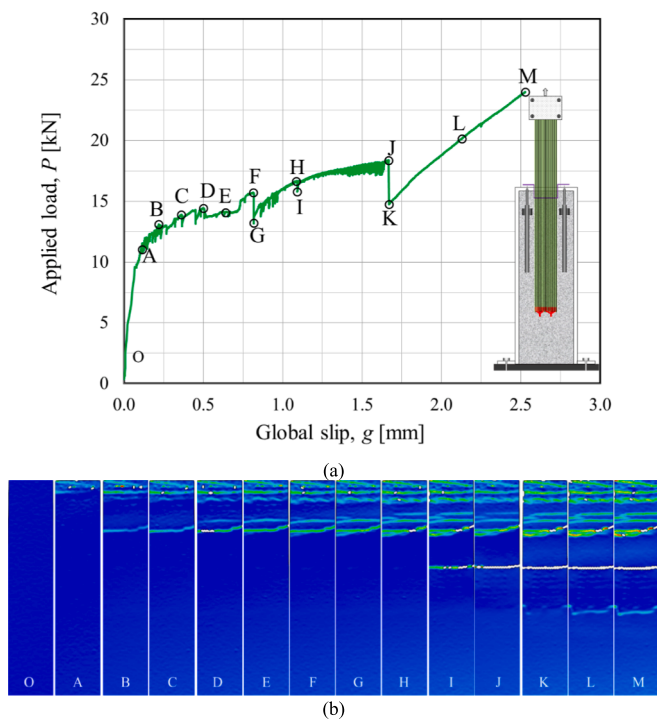
Furthermore, the anchor depth and fiber overlap length did not appear to have an effect on the peak load, as demonstrated when comparing the results of specimens S_80_1, S_80_2, and S_80_3.

The maximum global slip, g_{ult}, achieved by each specimen is listed in Table 2 and is shown in Fig. 16b. As expected, specimens with anchors near the loaded end (S_80_1, S_80_2, and S_80_3) had a much lower maximum global slip at failure compared to the unanchored (control) specimens C_1 and C_2. However, the anchored specimens with anchors located further from the loaded end (S_160, S_End_1, and S_End_2) exhibited a larger maximum global slip than the unanchored specimens. This further demonstrates that the load response of the anchored specimens is controlled by different mechanisms based on the location of the anchors. For the specimens with anchors near the loaded end, the steel fibers were activated early in the load response and controlled the maximum global slip. For the specimens with anchors farther from the loaded end, the interfacial cracking of the concrete substrate occurred over a longer length before the anchors were activated. The elastic elongation of the fibers along the debonded region caused larger global slip. The maximum global slip for specimen S_160 was smaller than that of the two specimens with end anchors (S_End_1 and S_End_2), although the difference is relatively small (approximately 0.2 mm). It can also be noted that the average maximum global slip of specimens S_End_1 and S_End_2 is roughly the same as the summation of the average maximum global slip of the unanchored specimens (C_1 and C_2) and that of the near-end anchored specimens (S_80_1, S_80_2, and S_80_3). This further demonstrates that the load response of the far-end anchored specimens is controlled by the composite and concrete substrate initially and then controlled by the steel fibers after complete debonding of the composite.

6. Numerical prediction of the load response

A finite difference method (FDM) was derived by the authors to predict the load response of fiber reinforced composite-concrete joints tested in direct shear [36]. The FDM numerically solves the following well-established governing equation [37,38]:
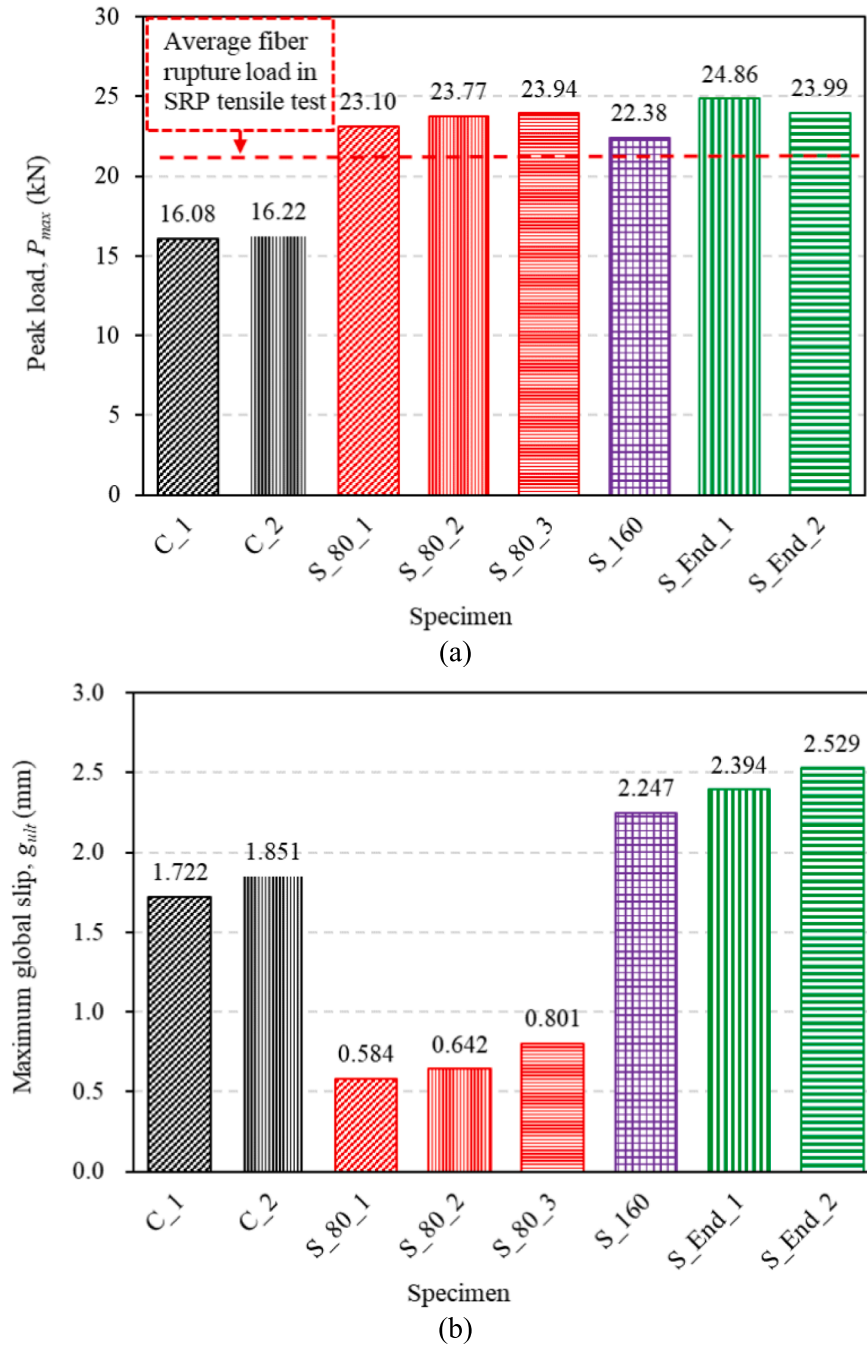
(a)

(b)

Fig. 16. Comparison of (a) peak applied load, and (b) maximum global slip.

$$\frac{d^2 s(x)}{dx^2} - \frac{\tau(s)}{E_f t_f} = 0 \tag{1}$$

where x is the coordinate along the bonded length, see Fig. 17. The boundary conditions at the unloaded (far) end are:

$$\varepsilon(y = 0) = 0 \tag{2a}$$

$$s(y = 0) = s_F \tag{2b}$$

where ε is the axial strain in the SRP plate, and s_F is the unloaded end slip.

6.1. Bond-slip relationship for bonded region and load-slip relationship for anchored region

In this study, a relationship between interface shear stress (τ) and the relative slip (s) between the composite and concrete was used to characterize the interface material. The interfacial cohesive material law developed by Dai et al. [36] was determined to characterize the SRP-concrete interface in the tests reported in [13] and the same SRP-concrete specimens in this study as:

$$\tau(s) = E_f t_f A^2 B \left(e^{-Bs} - e^{-2Bs} \right) \tag{3}$$

where $\tau(s)$ denotes the function of the cohesive material law, and E_f and t_f are the modulus of elasticity of the SRP and the equivalent thickness of
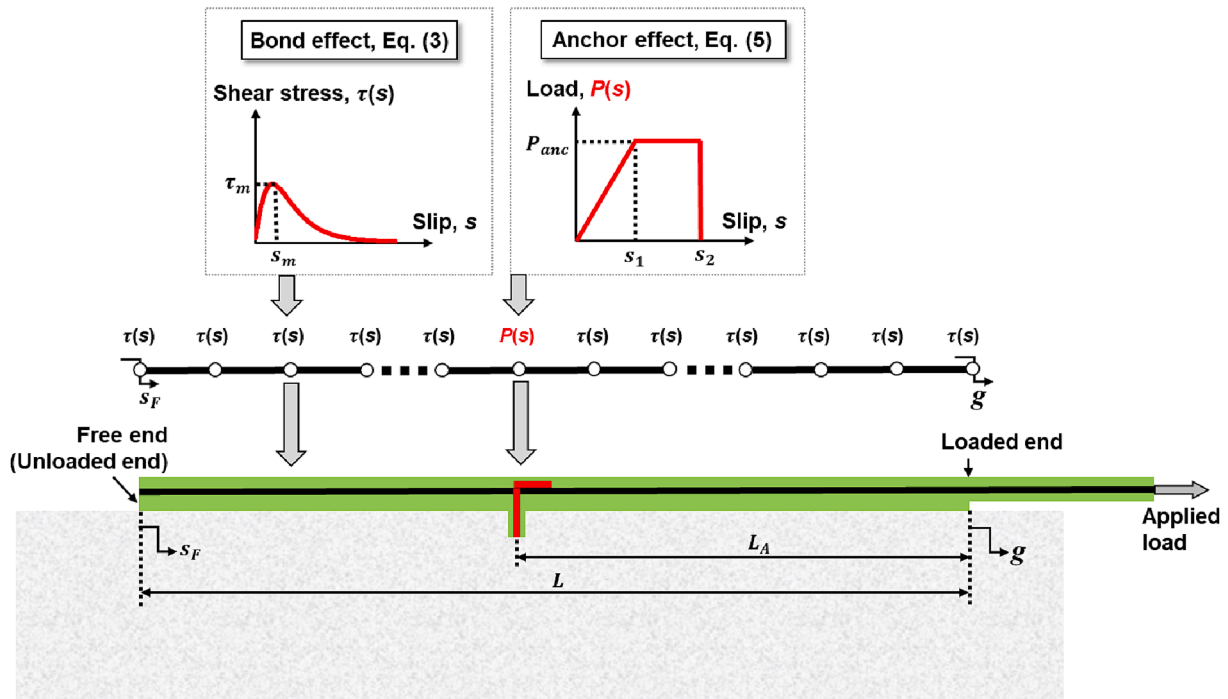
Fig. 17. Numerical model with bond-slip model for anchored and unanchored regions.

the fibers, respectively. The values of E_f and t_f are 257.2 GPa and 0.169 mm as discussed in **Sections 3.3 and 3.4**. A and B are parameters that define the peak value of shear stress and the shape of the $\tau(s)$ curve, which can be given as:

$$A = 2.4\sqrt{\frac{\tau_m s_m}{E_f t_f}} \tag{4a}$$

$$B = 0.693/s_m \tag{4b}$$

where τ_m and s_m are the maximum shear stress and the corresponding slip, respectively, see Fig. 17. The parameters of A and B were fitted with the experimental results for all MD fiber specimens that failed due to interfacial debonding in [13] as $A = 0.00725$ mm/mm and $B = 7.58$ /mm, with $R^2 = 0.996$. Solving Eq. (4) gives $s_m = 0.0915$ mm and $\tau_m = 4.386$ MPa as reported in [13].

For the anchored region, the load-slip relationship (see Fig. 17) was assumed to be similar to the relationship identified for spike-shaped anchors of CFRP fibers ([19,20]) as:

$$P(s) = \begin{cases} \frac{P_{anc}}{s_1}s, 0 \le s \le s_1 \\ P_{anc}, s_1 \le s \le s_2 \\ 0, s \ge s_2 \end{cases} \tag{5}$$

where $P(s)$ denotes the function of the relationship between the load of the anchor and the slip at the location of the anchor, P_{anc} is the maximum load that the anchors located at the same position along the bonded length can carry together (two anchors in this study), and s_1 and s_2 are the slips that mark the ends of the two stages in Eq. (5).

6.2. Numerical implementation

Introducing one of the bond-slip relationships of Eq. (3) into Eq. (1), the solution can be obtained from the following FDM approach. Central difference approximations of strain and the second order derivation of slip in Eq. (3) provide:

$$\varepsilon(y_i) = \frac{ds(y_i)}{dy} = \frac{s_{i+1} - s_{i-1}}{2h} \tag{6a}$$

$$\frac{d^2s(y_i)}{dy^2} = \frac{s_{i+1} - 2s_i + s_{i-1}}{h^2} \tag{6b}$$

where the discretization step (h) is $h = L/N$, L is the bonded length, and N is the number of discretizations. h is also the distance between consecutive points y_i, $i = 0, 1, 2, ..., N$, which is selected with N as the smallest integer above which no significant gain in accuracy can be detected.

Substituting Eq. (6b) into Eq. (1) and simplifying the results leads to:

$$s_{i+1} - 2s_i + s_{i-1} - \lambda\tau(s_i) = 0 \tag{7}$$

where $\lambda = h^2/(E_f t_f)$. Fig. 17 illustrates the numerical model discretized into nodes. For nodes without anchors, $\tau(s_i)$ is defined by Eq. (3). For the node with anchors, $\tau(s_i) = P(s)/(hb_f)$, as shown in Fig. 17, where b_f is the width of the bonded region. The boundary condition at the composite unloaded end is:

$$\varepsilon(0) = \frac{ds(0)}{dy} = 0 \tag{8}$$

Note that according to Eq. (8),

$$\varepsilon(0) = \frac{s_1 - s_{-1}}{2h} = 0 \tag{9}$$

Since s_{-1} is not within the domain, the solution is extended from the original domain of $[0, Nh]$ to $[-h, Nh]$. Therefore, the solution is given in $N+2$ nodes, where the first node is fictitious.

At the jth step, the solution of slip is given as the vector $\{s_i\}_j$, which meets the equilibrium condition of Eq. (7) and the boundary condition of Eq. (9). The increment of slip, i.e. the vector of $\{\delta s_i\}_{j+1}$, which is used to obtain the slip at the $(j+1)^{th}$ step as $\{s_i\}_{j+1} = \{s_i\}_j + \{\delta s_i\}_{j+1}$, can be computed from Eqs. (7) and (9):

$$\delta s_{i+1} - 2\delta s_i + \delta s_{i-1} - \lambda\tau(s_i + \delta s_i) = 0 \tag{10}$$

$$\frac{\delta s_1 - \delta s_{-1}}{2h} = 0 \tag{11}$$

The numerical solution is driven by increasing the global slip g. The boundary condition at the loaded end is:

$$\delta s_N = g_{inc} \tag{12}$$

where g_{inc} is the increase of g at each step. $\{\delta s_i\}_j$ can be obtained by solving the system of non-linear equations comprising Eqs. (10)-(12):

$$\begin{cases} \delta s_1 - \delta s_{-1} = 0 \\ \delta s_{i+1} - 2\delta s_i + \delta s_{i-1} - \lambda\tau(s_i + \delta s_i) = 0, \ i = 0, 1, 2, \cdots, N-1 \\ \delta s_N = g_{inc} \end{cases} \tag{13}$$

The nonlinear Eq. (13) can be solved by a modified Newton-Raphson iteration technique as:

$$\{\delta s_i\}_{j+1}^{k+1} = \{\delta s_i\}_{j+1}^{k} - J^{-1}\left(\{\delta s_i\}_{j+1}^{k}\right)\{f_i(g_{inc})\} \tag{14}$$

where $\{\delta s_i\}_{j+1}^{k}$ refers to the kth sub-step of the iteration within the computation of the increment of slip at the $(j+1)^{th}$ step, $\{\delta s_i\}_{j+1}$. $J(\delta s_i)$ is the Jacobian matrix for this system, $J^{-1}(\delta s_i)$ is the inverse of $J(\delta s_i)$, and $\{f_i(g_{inc})\}$ is the right side of Eq. (13). From the jth step to the $(j+1)^{th}$ step, the increase of slip vector, $\{\delta s_i\}_{j+1}$, is updated using Eq. (14) until

the convergence criterion is met:

$$\frac{\left|\{\delta s_i\}_{j+1}^{k+1} - \{\delta s_i\}_{j+1}^{k}\right|}{\left|\{\delta s_i\}_{j+1}^{k}\right|} \leq \epsilon \tag{15}$$

where ϵ is the tolerance, taken equal to 10^{-6} in this study.

It should be noted that the FDM solution can capture the snap-back phenomenon when the solution is driven by monotonically increasing the unloaded end slip [36]. However, the direct shear tests in this study were controlled by monotonically increasing the global (i.e., loaded end) slip, so the snap-back phenomenon could not be captured experimentally. Accordingly, the numerical simulation is herein terminated when the global slip results in a dramatic load decrease or when the applied load reaches the load corresponding to fiber rupture.

Once the slip distribution is determined, the shear stress can be determined by Eq. (3) as:

$$\tau_i = \tau(s_i) \tag{16}$$

The applied load is computed enforcing the equilibrium of the composite strip:

$$P = E_f b_f t_f \varepsilon_N \tag{17}$$

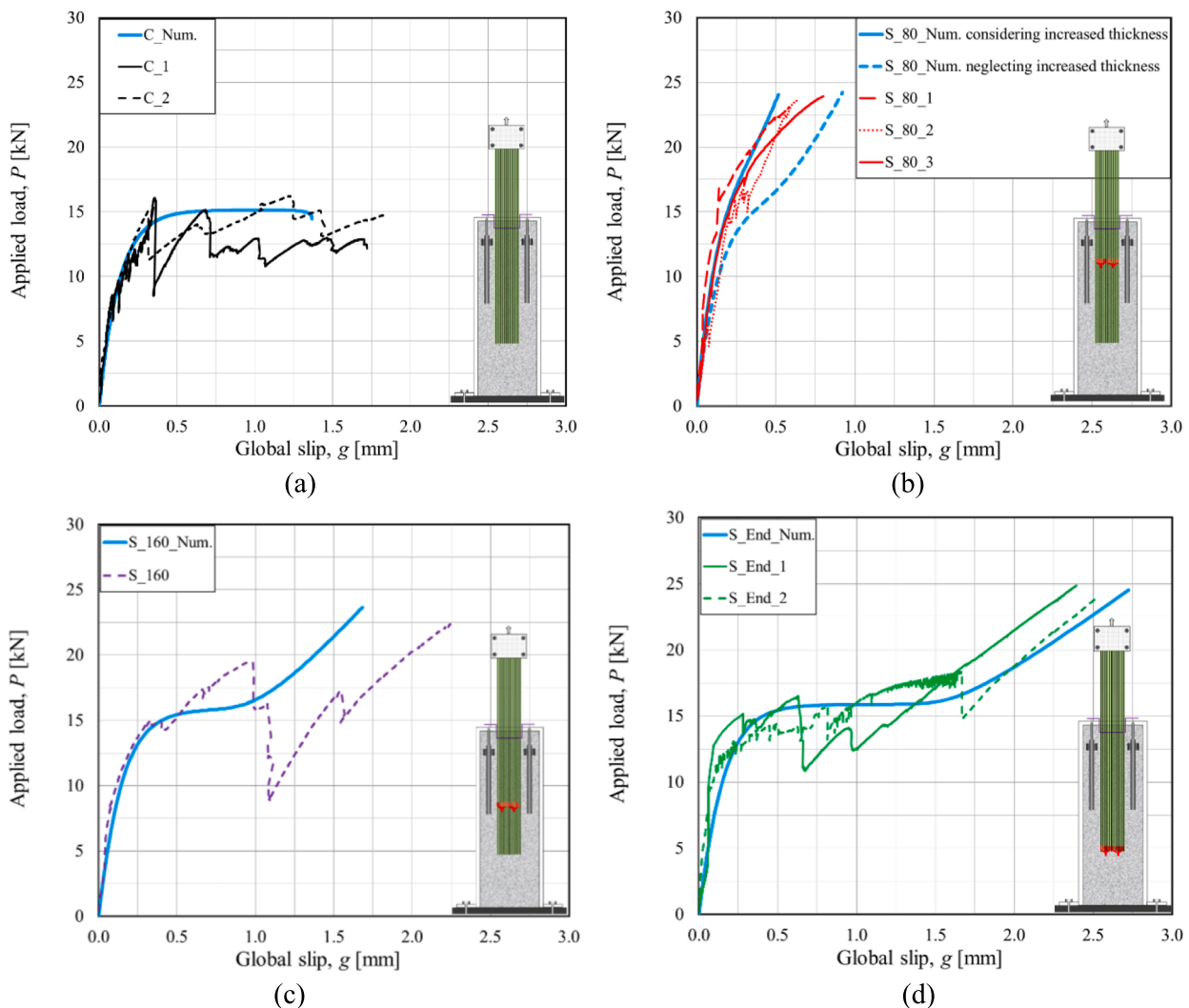where ε_N is the strain at the loaded end. Additional details of the FDM

Fig. 18. Comparison between numerical and experimental results: (a) control specimens, (b) anchored specimens with $L_A = 80$ mm, (c) anchored specimens with $L_A = 160$ mm, and (d) anchored specimens at unloaded end.

solution are presented in [36].

6.3. Comparison between numerical and experimental results

The accuracy of the FDM method in **Section 6.2** was validated in [36] for analytical and experimental results of FRP-concrete direct shear specimens without anchors. The FDM method matched well with the analytical results proposed in [39,40] for producing the *P-g* response. **Fig. 18a** compares the *P-g* curves determined by FDM and the experimental results of the unanchored (control) specimens in this study. It can be seen that the numerical and experimental results matched well.

To simulate the response of the anchored specimens, the mechanical properties of the anchors are needed, however, these properties have not been tested. As a first step, it is hypothesized that the spike-shaped anchorage proposed in this study works in the same manner as CFRP spike anchors do in [20]. Considering the linearly increasing nature of the anchored specimens' load responses along with the fiber rupture failure mode that occurred, only the initial slope $\frac{P_{anc}}{s_1}$ of the *P(s)* curve (first piece of Eq. (5)) should affect the simulation results of the specimens considered. For the sake of illustration, as a first step, *P(s)* models of different fiber anchors from the literature were considered. The values adopted in Eq. (5) of $P_{anc} = 21.60$ kN (i.e., the tensile strength of the SRP plate, see **Section 3.3**) and $s_1 = 0.0915$ mm (i.e., s_m, see **Section 6.1**) were found to provide results that were in reasonable agreement with the experimental results. Finally, s_2 was set to a value that was sufficiently large (2.0 mm in this study). The method herein is intended to validate the overall approach and can be further refined when more data on the mechanical properties of the SRP fiber anchors become available.

Using the assumed values of P_{anc} and s_1, **Fig. 18b, c, d** show that the numerical simulation matched well with the experimental results of the anchored specimens herein tested. In the case of the near-end anchored specimens, with $L_A = 80$ mm, **Fig. 18b** shows that considering the effect of the increased thickness in the anchored overlap zone resulted in a better prediction of the load response, i.e., smoother transition from being controlled by the composite and substrate to the fibers discussed in **Section 5.3**, compared with neglecting the thickness increase. The reason is that for these specimens, the fiber overlapped (length d_1) extended along a significant portion of the bonded length between the loaded end and the anchor. For other anchored specimens, when the overlapped length is much shorter than the bonded length between the loaded end and the anchor, the increased thickness was neglected. **Fig. 18c** shows that the simulation of anchored specimens with $L_A = 160$ mm matched well with the experimental results for $g \leq 0.6$ mm, but after that the experimental curve showed a large fluctuation. **Fig. 18d** shows that the load response of the far-end anchored specimens were well predicted. It should be noted that for *g* greater than 1.75 mm, both the numerical and experimental results show a linear increase stage of the curve, which is due to the elastic elongation of the detached SRP strip. Better agreement may be obtained when results of mechanical tests of SRP anchors are available.

Fig. 19 shows the numerical prediction of applied load-global slip curves for anchored specimens with $L_A = 80$ mm, 120 mm, 160 mm, 200 mm, and 240 mm. It can be seen that with the increase of L_A, and therefore of the bonded length at the loaded end, the specimens have the same failure load, corresponding to fiber rupture, and the global slip at failure increases. Herein it is conjectured that the upward tail of the curves (from around 18 kN to the failure) is caused mainly by elongation of the fiber strip from the anchor to the loaded end, which can be computed using the following equation:

$$E_{eq} = \left(\frac{\Delta P}{b_f t_f}\right) \Big/ \left(\frac{\Delta g}{L_A}\right) \tag{18}$$

where E_{eq} is the equivalent modulus of the debonded SRP, and ΔP and Δg are the load and global slip (elongation) increase from 18 kN to the failure. **Fig. 19** shows that E_{eq} is close to but slightly lower than the
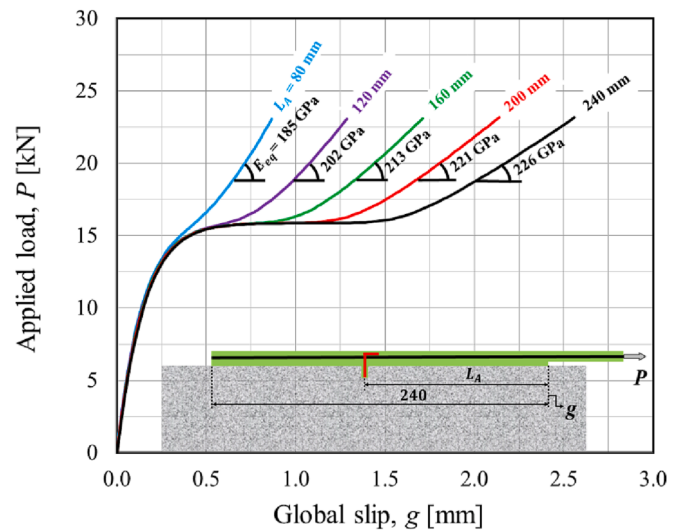

Fig. 19. Numerical prediction of applied load-global slip curves for specimens with $L_A = 80$ mm, 120 mm, 160 mm, 200 mm, and 240 mm.

modulus of the SRP plate (257.2 GPa in **Section 3.4**), indicating the deformation in that region of the response is caused mainly by the elongation of the fiber.

Fig. 20a and **20b** show the predicted applied load-global slip curve for unanchored and end-anchored specimens, with bonded length longer than the effective length respectively. It can be seen that the end-anchored specimen has a higher ultimate capacity and substantially more ultimate global slip than the unanchored specimen. **Fig. 20c** and **20d** show the mechanical response of and slip, axial strain, and shear stress distribution along the bonded length for Points A-H of the corresponding load response in **Fig. 20a** and **20b**. For the unanchored case, **Fig. 20a** shows that the global slip exhibited a linear response after Point D, because that the axial strain reaches a plateau at the same load level. The shear stress continued to translate from the loaded end to the free end until failure of the specimen. The results in **Fig. 20b** illustrate that the load response of the anchored specimens can be divided into three stages: the initial debonding stage, the debonding stage (the plateau in **Fig. 20b**) and the anchoring stage (the linear branch in **Fig. 20b**). The initial debonding stage and the debonding stage were also observed experimentally in **Fig. 18a**. The anchoring stage is a new finding herein, which shows the anchor will take action only when the slip at the anchor is large enough to "activate" itself.

7. Conclusion

This work presents an experimental and numerical procedure to determine the performance of a novel anchorage system for SRP-concrete joints based on experimental data acquired from single-lap direct shear test specimens. The following conclusions are drawn:

(1) Unanchored (control) specimens failed due to SRP-concrete debonding, while anchored specimens failed due to fiber rupture with much higher load capacity. The spike anchors enabled full utilization of the SRP material strength.

(2) The spike anchors can substantially increase the peak load of the SRP-concrete joint with respect to the unanchored specimens. For the specimens in this study, a 40% to 50% increase was observed.

(3) The location of the anchorage influenced the load responses. The load response of near-end anchored specimens was controlled mainly by the fibers until failure. The load response of far-end anchored specimens was controlled by the composite and substrate until the composite completely debonded, after which it was controlled by the fibers until failure. The closer the anchor is
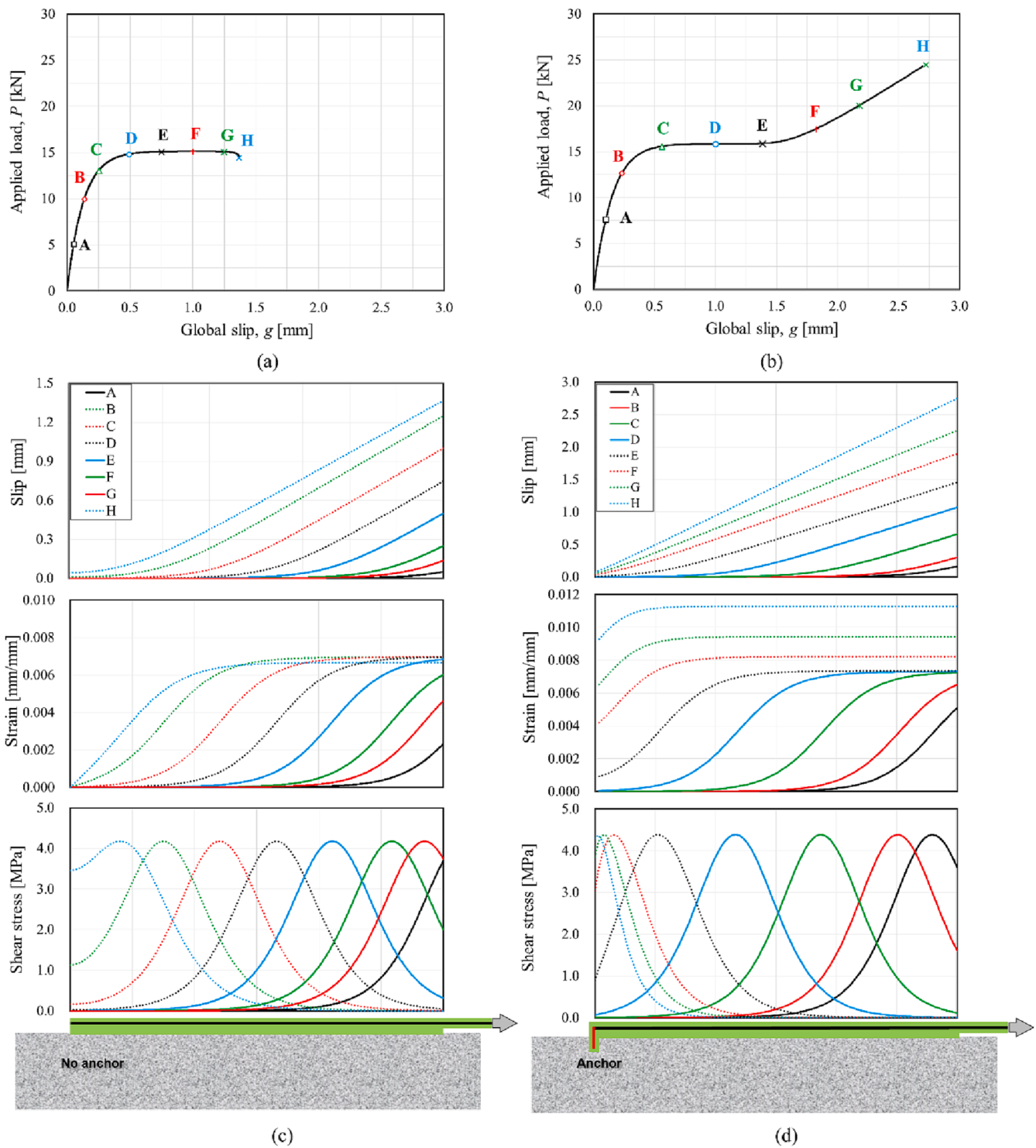
Fig. 20. Predicted load response: (a) and (b) are applied load-global slip curve with marked Points A-H for unanchored and anchored specimens, respectively, (c) and (d) are slip, strain, and shear stress distribution along the bonded length points on the applied load-global slip responses of unanchored and anchored specimens, respectively.

to the loaded end, the less global slip was reached when the load reached the peak value.

(4) The numerical procedure based on the FDM approach proposed by the authors can accurately predict the full-range behavior of unanchored and anchored specimens. In the case where the anchor is close to the loaded end ($L_A = 80$ mm), the prediction accuracy was increased when the increased thickness of the SRP strip caused by the anchor was considered.

(5) The load response of the anchored specimens can be divided into three stages: the initial debonding stage, the debonding stage, and the anchoring stage. The anchoring stage is a new finding and indicates that the anchor will engage only when the bonded region adjacent to the anchor debonded to "activate" itself.

This study is the first step to present the concept of the proposed spike anchor system for SRP. More test data are needed in the future to

determine the mechanical properties of the SRP anchors and to study the influence of different parameters such as fiber density and anchor configuration.

Funding

This research did not receive any specific grant from funding agencies in the public, commercial, or not-for-profit sectors.

Declaration of Competing Interest

The authors declare that they have no known competing financial interests or personal relationships that could have appeared to influence the work reported in this paper.

Data availability

The raw/processed data required to reproduce these findings cannot be shared at this time as the data also forms part of an ongoing study.

References

[1] C.E. Bakis, L.C. Bank, V. Brown, E. Cosenza, J.F. Davalos, J.J. Lesko, A. Machida, S. H. Rizkalla, T.C. Triantafillou, Fiber-reinforced polymer composites for construction-State-of-the-art review, J Compos Constr 6 (2) (2002) 73–87, https://doi.org/10.1061/(ASCE)1090-0268(2002)6:2(73).

[2] Y. Tang, G. Wu, Z. Sun, Seismic performance of underwater bridge columns strengthened with prestressed-concrete panels and FRP reinforcement, J Compos Constr 23 (3) (2019) 04019019, https://doi.org/10.1061/(ASCE)CC.1943-5614.0000948.

[3] Y. Wei, C. Zhu, K. Miao, K. Zheng, Y. Tang, Compressive performance of concrete-filled steel tube columns with in-built seawater and sea sand concrete-filled FRP tubes, Const Build Mat 317 (2022), 125933, https://doi.org/10.1016/j.conbuildmat.2021.125933.

[4] Wobbe E., Silva P., Barton B.L., Dharani L.R., Birman V., Nanni A., Alkhrdaji T., Thomas J., Tunis T. Flexural capacity of R/C beams externally bonded with SRP and SRG. In: Proc. of Society for the Advancement of Material and Process Engineering Symp. Long Beach, CA, USA; 2004. p. 20–7.

[5] A. Lopez, N. Galati, T. Alkhrdaji, A. Nanni, Strengthening of a reinforced concrete bridge with externally bonded steel reinforced polymer (SRP), Compos Part B: Eng 38 (4) (2007) 429–436, https://doi.org/10.1016/j.compositesb.2006.09.003.

[6] P. Casadei, A. Nanni, T. Alkhrdaji, J. Thomas, Performance of double-T prestressed concrete beams strengthened with steel reinforcement polymer, Adv Struct Eng 8 (4) (2005) 427–442, https://doi.org/10.1260/136943305774353124.

[7] L.H. Sneed, S. Verre, L. Ombres, C. Carloni, Flexural behavior RC beams strengthened and repaired with SRP composite, Eng Struc 258 (2022), 114084, https://doi.org/10.1016/j.engstruct.2022.114084.

[8] W. Figeys, L. Schueremans, D. Van Gemert, K. Brosens, A new composite for external reinforcement: Steel cord reinforced polymer, Const Build Mat 22 (9) (2008) 1929–1938, https://doi.org/10.1016/j.conbuildmat.2007.07.006.

[9] M. Pecce, F. Ceroni, A. Prota, G. Manfredi, Response prediction of RC beams externally bonded with steel-reinforced polymers, J Compos Constr 10 (3) (2006) 195–203, https://doi.org/10.1061/(ASCE)1090-0268(2006)10:3(195).

[10] G. Baietti, S.K. Shahreza, M. Santandrea, C. Carloni, Concrete columns confined with SRP: Effect of the size, cross-sectional shape and amount of confinement, Const Build Mat 275 (2021), 121618, https://doi.org/10.1016/j.conbuildmat.2020.121618.

[11] Y. Wei, Y. Wu, Compression behavior of concrete columns confined by high strength steel wire, Const Build Mat 54 (2014) 443–453, https://doi.org/10.1016/j.conbuildmat.2013.12.083.

[12] Kim J.Y., Fam A., Kong A., El-Hacha R. Flexural strengthening of RC beams using steel reinforced polymer (SRP) composites. In: Proc. of the 7th Int. Symp. FRP reinforcement for concrete structures, ACI SP-230, 1, Paper #93; 2005; p. 1647–64.

[13] X. Zou, L.H. Sneed, Bond behavior between steel fiber reinforced polymer (SRP) and concrete, Int J Concr Struct Mater 14 (1) (2020) 1–17, https://doi.org/10.1186/s40069-020-00420-1.

[14] F. Ascione, M. Lamberti, A. Napoli, G. Razaqpur, R. Realfonzo, An experimental investigation on the bond behavior of steel reinforced polymers on concrete substrate, Compos Struct 181 (2017) 58–72, https://doi.org/10.1016/j.compstruct.2017.08.063.

[15] C. Carloni, M. Santandrea, I.A.O. Imohamed, Determination of the interfacial properties of SRP strips bonded to concrete and comparison between single-lap and

[16] notched beam tests, Eng Frac Mech 186 (2017) 80–104, https://doi.org/10.1016/j.engfracmech.2017.09.020.

[16] D. Mostofinejad, E. Mahmoudabadi, Grooving as alternative method of surface preparation to postpone debonding of FRP laminates in concrete beams, J Compos Constr 14 (6) (2010) 804–811, https://doi.org/10.1061/(ASCE)CC.1943-5614.0000117.

[17] P. Zhang, H. Zhu, G. Wu, S.P. Meng, Z.S. Wu, Shear capacity comparison of four different composite interfaces between FRP plates and concrete substrate, J Compos Constr 20 (4) (2016) 04016006, https://doi.org/10.1061/(ASCE)CC.1943-5614.0000666.

[18] R. Kalfat, R.A. Mahaidi, Improvement of FRP-to-concrete bond performance using bidirectional fiber patch anchors combined with FRP spike anchors, Compos Struct 155 (2016) 89–98, https://doi.org/10.1016/j.compstruct.2016.08.010.

[19] H.W. Zhang, S.T. Smith, Influence of FRP anchor fan configuration and dowel angle on anchoring FRP plates, Compos Part B: Eng 43 (8) (2012) 3516–3527, https://doi.org/10.1016/j.compositesb.2011.11.072.

[20] H. Zhang, S.T. Smith, R.J. Gravina, Z. Wang, Modelling of FRP-concrete bonded interfaces containing FRP anchors, Const Build Mat 139 (2017) 394–402, https://doi.org/10.1016/j.conbuildmat.2017.02.080.

[21] S.V. Grelle, L.H. Sneed, Review of anchorage systems for externally bonded FRP laminates, Int J Concr Struct Mater 7 (1) (2013) 17–33, https://doi.org/10.1007/s40069-013-0029-0.

[22] K. Galal, M. Sekar, Rehabilitation of RC inverted-T girders using anchored CFRP sheets, Compos Part B: Eng 39 (4) (2008) 604–617, https://doi.org/10.1016/j.compositesb.2007.09.001.

[23] P. Mahrenholtz, J.M. Park, J.Y. Cho, Monotonic and cyclic behaviour of isolated FRP anchors loaded in shear, Compos Part B: Eng 72 (2015) 72–79, https://doi.org/10.1016/j.compositesb.2014.11.033.

[24] R. Kalfat, R. Al-Mahaidi, Investigation into bond behaviour of a new CFRP anchorage system for concrete utilising a mechanically strengthened substrate, Compos Struct 92 (11) (2010) 2738–2746, https://doi.org/10.1016/j.compstruct.2010.04.004.

[25] J.G. Dai, T. Yokota, T. Ueda, A hybrid bonding system for improving the structural performance of FRP flexurally strengthened concrete beams, Adv Struct Eng 12 (6) (2009) 821–832, https://doi.org/10.1260/136943309790327671.

[26] B. Fu, X.T. Tang, L.J. Li, F. Liu, G. Lin, Inclined FRP U-jackets for enhancing structural performance of FRP-plated RC beams suffering from IC debonding, Compos Struct 200 (2018) 36–46, https://doi.org/10.1016/j.compstruct.2018.05.074.

[27] A. Balsamo, F. Nardone, I. Iovinella, F. Ceroni, M. Pecce, Flexural strengthening of concrete beams with EB-FRP, SRP and SRCM: Experimental investigation, Compos Part B: Eng: Engineering 46 (2013) 91–101, https://doi.org/10.1016/j.compositesb.2012.10.014.

[28] Y. Zhou, X. Wang, L. Sui, F. Xing, Y. Wu, C. Chen, Flexural performance of FRP-plated RC beams using H-type end anchorage, Compos Struct 206 (2018) 11–21, https://doi.org/10.1016/j.compstruct.2018.08.015.

[29] ASTM C39, C39M-17b. Standard test method for compressive strength of cylindrical concrete specimens 2021 ASTM International. PA, USA West Conshohocken, Pam 7.

[30] Astm c496, c496m. Standard Test Method for Splitting Tensile Strength of Cylindrical Concrete Specimens 2017 ASTM International. PA, USA West Conshohocken, Pam 5.

[31] ECO Products of Kerakoll: products.kerakoll.com (accessed on June 2022).

[32] GOM Correlate: https://www.gom.com/ (accessed on June 2022).

[33] J.F. Chen, J.G. Teng, Anchorage strength models for FRP and steel plates bonded to concrete, J Struct Eng 127 (7) (2001) 784–791, https://doi.org/10.1061/(ASCE)0733-9445(2001)127:7(784).

[34] X.Z. Lu, J.G. Teng, L.P. Ye, J.J. Jiang, Bond-slip models for FRP sheets/plates bonded to concrete, Eng Struc 27 (6) (2005) 920–937, https://doi.org/10.1016/j.engstruct.2005.01.014.

[35] J.P. Lin, Y.F. Wu, Numerical analysis of interfacial bond behavior of externally bonded FRP-to-concrete joints, J Compos Constr 20 (5) (2016) 04016028, https://doi.org/10.1061/(ASCE)CC.1943-5614.0000678.

[36] X. Zou, T. D'Antino, L.H. Sneed, Investigation of the bond behavior of the fiber reinforced composite-concrete interface using the finite difference method (FDM), Compos Struct 278 (2021) 114643, https://doi.org/10.1016/j.compstruct.2021.114643.

[37] J. Dai, T. Ueda, Y. Sato, Development of the nonlinear bond stress–slip model of fiber reinforced plastics sheet–concrete interfaces with a simple method, J Compos Constr 9 (1) (2005) 52–62, https://doi.org/10.1061/(ASCE)1090-0268(2005)9:1(52).

[38] K. Liu, Y.F. Wu, Analytical identification of bond–slip relationship of EB-FRP joints, Compos Part B: Eng 43 (4) (2012) 1955–1963, https://doi.org/10.1016/j.compositesb.2012.01.048.

[39] H. Yuan, J.G. Teng, R. Seracino, Z.S. Wu, J. Yao, Full-range behavior of FRP-to-concrete bonded joints, Engineering Structures 26 (5) (2004) 553–565, https://doi.org/10.1016/j.engstruct.2003.11.006.

[40] L. He, Y.F. Wu, Y. Xiao, Analytical solution for externally bonded joints considering snap-back, Journal of Composites for Construction 19 (5) (2015) 04014077, https://doi.org/10.1061/(ASCE)CC.1943-5614.0000542.